Acta Materialia 263 (2024) 119498

Contents lists available at ScienceDirect

Acta Materialia

journal homepage: www.elsevier.com/locate/actamat

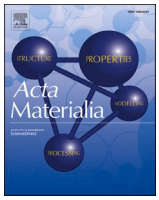

Full length article

Transient to steady-state morphology evolution of carbon surfaces under ion bombardment: Monte Carlo simulations

H. Tran, H.B. Chew *

Department of Aerospace Engineering, University of Illinois at Urbana-Champaign, Urbana IL 61801, USA

ARTICLE INFO

Keywords:
Carbon sputtering
Surface morphology
Sputtering-by-design
Sputtering yield
Monte Carlo simulations

ABSTRACT

Molecular dynamics (MD) simulations have established the sputtering yields of carbon under the low-energy bombardment of noble gas ions. Here, we upscale these MD results to account for the evolving surface morphology and sputtering yield with ion fluence using a Monte Carlo model, which considers the shadowing of the incident ion flux, redeposition of sputtered carbon material, and secondary sputtering induced by the surface impact of carbon sputterants. Results show that initially rough surface morphologies are consistently smoothened and flattened by a normal ion flux, resulting in sputtering yields that approach MD predictions. Under a highly oblique ion flux, however, the activation of multiple cooperative roughening and smoothening mechanisms at different scales lead to the formation of characteristic surface steps at the microscale, with steady-state sputtering yields that are up to an order-of-magnitude lower than MD predictions. While the observed surface features and the ensuing sputtering yield at steady-state are generally not sensitive to the initial surface morphology, the initial morphology controls the ion fluence to attain steady-state. We discuss surface design strategies to delay and abate sputtering.

1. Introduction

Sputtering is the physical process of removing atoms from a material surface by bombardment with energetic ions, and is widely adopted for surface patterning [1], etching of holes [2–6], as well as material removal for subsequent thin film deposition on substrates [7,8]. However, sputtering is generally undesirable for plasma-facing materials, since it erodes the surfaces of critical material components and alters the plasma operational conditions [9–11]. Because of its remarkable sputter-resistant properties, carbon is often the material of choice to coat the critical surfaces of plasma devices, including the pole covers of Hall-effect thrusters, accelerator grids in ion thrusters, and the divertor within magnetic fusion devices [12–16]. Sputtering-induced erosion of the carbon coatings under a high ion fluence eventually leads to failure of these devices, but is challenging to quantify both experimentally and computationally in view of the very low sputter yield of carbon.

In spacecraft electric propulsion devices, for example, the carbon coatings are subjected to xenon ion bombardment with low ion energies of 100 to 1000 eV and at high ion fluence of 10^{20} to 10^{30} ions/cm^2 [13,14], which necessitates significant ground-based experimental runtimes of at least 4 to 12 h to achieve quantifiable sputter yield for a conventional ion source [16–18]. This contributes to the large uncertainties in the sputtering yield measurements of carbon reported across different laboratories in the past couple of decades, particularly under low ion energies where the reported values could differ by an order of magnitude [17–24]. While these sputtering studies were performed on different allotropes of carbon, including diamond, amorphous carbon, pyrolytic and isotropic graphite, as well as carbon-carbon composites, recent molecular dynamics (MD) simulations show that the steady-state sputtering yield is independent of both the initial carbon structure and prior sputtering history, in agreement with sputtering experiments [25]. This is attributed to the rapid amorphization of the carbon subsurface with ion bombardment, which resulted in virtually indistinguishable amorphous structures across a wide range of ion energies, ion incidence angles, and initial carbon structures. Instead, the measured sputtering yield may be sensitive to surface roughness, as evidenced by surface texturing on carbon films with height variations (amplitudes) of ~0.2 μm [22,26] (Fig. 1a), as well as changes in the measured sputtering yield with evolving surface morphology of exposed carbon fibers [17].

Early theoretical studies of surface erosion by ion bombardment generally assume that the sputtering yield is independent of surface

* Corresponding author.
E-mail address: hbchew@illinois.edu (H.B. Chew).

https://doi.org/10.1016/j.actamat.2023.119498
Received 15 June 2023; Received in revised form 15 October 2023; Accepted 3 November 2023
Available online 7 November 2023

curvature effects [27]. Later analytical developments by Bradley and Harper consider the effects of surface instability caused by curvature dependence, where the sputter yield is greater in a trough than at a crest [28,29]; these models have successfully predicted a wide range of nanoscale surface structures induced by ion bombardment – from nanoripples to quantum dots [30,31]. However, curvature effects are only apparent at high ion energies (>∼ 5 keV) and at very small wavelength (<∼ 100 nm) where the impact-induced damage can span across multiple nanoripples [31–33]. At lower ion energies of 100 to 1000 eV relevant to spacecraft electric propulsion, the variations of the sputtering yield and differential yield profile with *microscale* surface roughness wavelength of ∼ 2 μm (Fig. 1a) [22] can be primarily attributed to: (a) changes in the local incidence angle at the impact site, which also alters the trajectory of the sputterants, (b) impact of sputterants with surface features to cause deposition or the emission of secondary sputterants, and (c) partial shielding of the surface from incoming ions by surface features leading to a shadowing or masking effect. Accounting for these contributions and allowing the surface morphology to evolve with sputtering are beyond the length- and time-scales of MD simulations. To this end, Monte Carlo methods based on binary collision approximation are widely used to model surface evolution [30,34–39], while maintaining the ability to account for sputtering mechanisms typically neglected in analytical and continuum-based view factor sputtering models [40–43], such as secondary sputtering caused by surface impact of the sputterants [29,44]. However, the binary collision approximation in these Monte Carlo methods are well-known to break down at low ion energies of <∼ 1 keV [45–49].

Previously, we performed large-scale, massively-parallel MD simulations to quantify the sputtering yield and differential yield profile for the bombardment of xenon ions on carbon substrates across a wide range of ion energies (75 eV to 2 keV) and incidence angles (0° to 75°) [25]. In this work, we extend the length- and time-scales of these MD simulations through a Monte Carlo model to elucidate the ion-surface sputtering mechanisms, evolving surface morphology, and resulting sputtering yield associated with *microscale* surface roughness (Fig. 1a) under sputtering conditions relevant to spacecraft electric propulsion. Section 2 describes the Monte Carlo modeling approach and the underlying MD-derived sputtering characteristics. We detail in Section 3 the fundamental ion-surface erosion and deposition mechanisms leading to surface texturing under normal and oblique ion incidence angles and present the transient and steady-state sputtering yields associated with the evolving surface morphologies in Section 4. We expand our Monte Carlo simulations to include a wide range of initial surface morphologies in Section 5, and explore design strategies to control and abate sputtering by surface texturing. Finally, we discuss the implications of our Monte Carlo simulations in the context of prior experiments and conclude with a summary in Section 6.

2. Simulation methodology

Studies focusing on nanoscale texturing have uncovered several

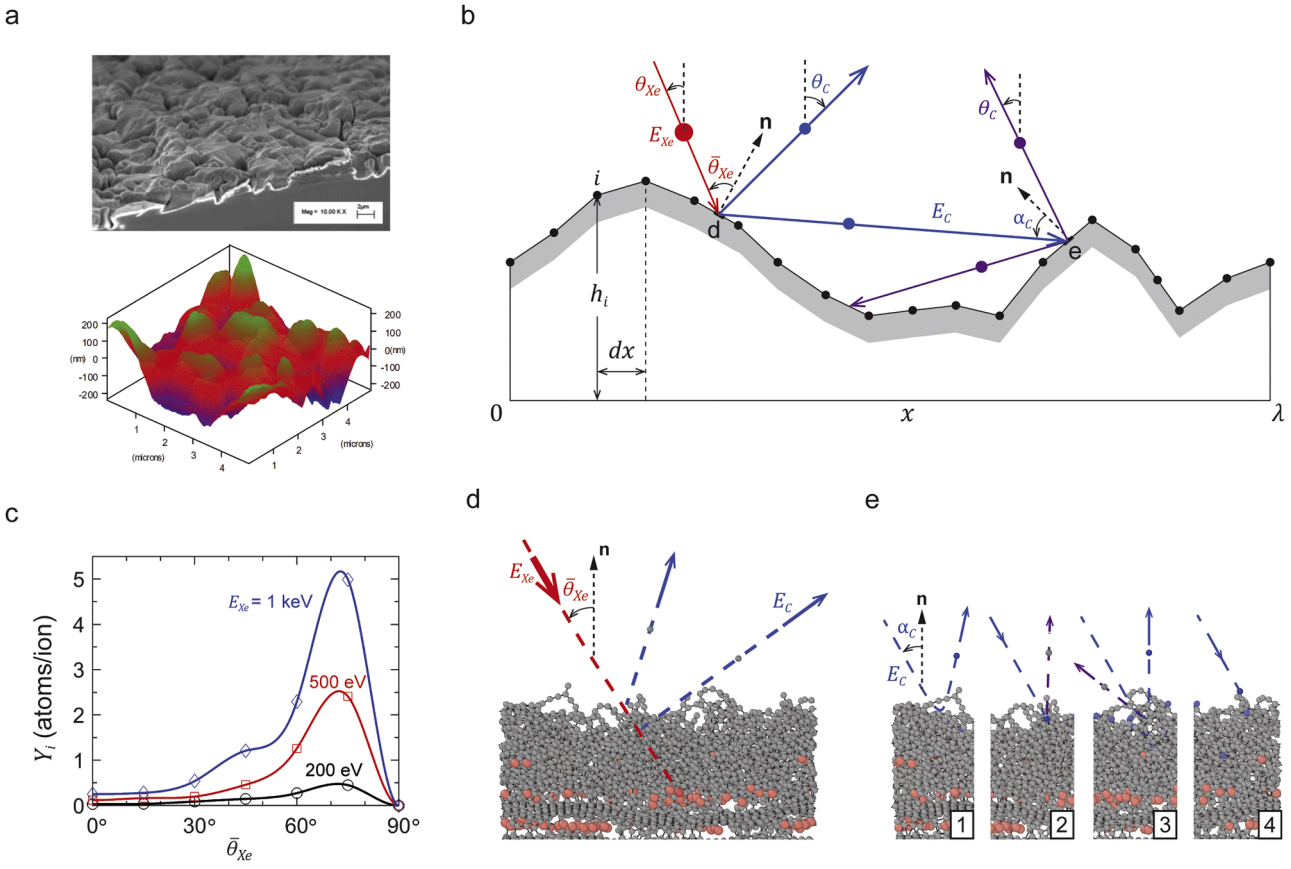

Fig. 1. **(a)** Surface morphology of amorphous carbon characterized by scanning electron microscopy (SEM) and atomic force microscopy (AFM) imaging [22]. **(b)** Monte Carlo modeling of sputtering erosion caused by the impingement of xenon ions (red) on an undulating carbon surface, knocking-off primary (blue) and secondary (purple) carbon sputterants. **(c)** Elemental sputtering yield (Y_i) as a function of local ion incidence angle, $\bar{\theta}_{Xe}$, for three ion incidence energies, E_{Xe} = 200, 500, 1000 eV; symbols denote the steady-state sputtering yield from molecular dynamics (MD) simulations connected with a spline fitting, with exception for $\bar{\theta}_{Xe}$ = 90° where Y_i = 0 is assumed. **(d,e)** MD simulations of the energetic bombardment of amorphous carbon substrates with xenon ions (**d**) and carbon atoms (**e**), to quantify the sputtering characteristics of primary (**d**) and secondary carbon sputterants (**e**), which govern the underlying elemental properties of the Monte Carlo model.

physical phenomena that can significantly influence surface morphology evolution and surface patterning at the nanoscale (roughness wavelength of <100 nm), including ion-induced mass redistribution, curvature-dependent sputtering, and ion-induced viscous flow [30,50,51]. In particular, mass redistribution is an important destabilizing effect that contributes to the formation of nanoscale surface ripples for sufficiently high angles of ion incidence [50,52]. Our previous MD simulations on the sputtering of carbon surfaces also reveal that both ion-induced mass redistribution and ion-induced viscous flow contribute to rapid amorphization of the carbon subsurface, but the structural characteristics ($sp/sp^2/sp^3$ bond proportions, atomic density) eventually plateau once "steady-state" bombardment of the MD simulation box (with 5×5 nm^2 exposed surface to the incident ions) is attained at the time-scale of $\sim 10^{15}$ ions/cm^2 [25]. This time-scale is several orders of magnitude smaller than the time-scale required to evolve the carbon surfaces with micron-scale undulations (Fig. 1a) to reach steady-state in experiments ($\sim 10^{19}$ to 10^{20} ions/cm^2) [17,18], which is the focus of our studies. This time-scale separation allows us to delineate the local nanoscale effects of ion-induced mass redistribution and viscous flow from microscale surface morphology evolution.

Here, we homogenize the nanoscale sputtering response from MD [25], and consequently, the physical effects of ion-induced mass redistribution and viscous flow, into a single representative element in our kinetic Monte Carlo approach, where the sputtering yield of each element is based on the steady-state sputtering response from MD. In this homogenized framework outlined in Fig. 1b, the impingement of an incoming xenon ion on a carbon surface will cause the emission of (primary) carbon sputterants (blue arrows), which can escape from the surface, or impact with other surface features and potentially trigger the emission of secondary carbon sputterants (purple arrows). In turn, this process can trigger the emission of tertiary carbon sputterants. However, the secondary carbon sputterants tend to get absorbed upon impact with surface features due to their low energies ($\sim$1 eV). Our kinetic Monte Carlo approach simulates the evolving surface morphology from two competing mechanisms: (i) surface recession due to sputtering induced by surface impact of xenon ions and primary carbon sputterants, and (ii) surface growth due to deposition of primary and secondary carbon sputterants.

Scanning electron microscopy (SEM) and atomic force microscopy (AFM) measurements of amorphous carbon structures (Fig. 1a) show the surfaces to have height variations (amplitudes), $\frac{H}{2}$, of $\sim$200 nm, with microscale roughness wavelength, λ, of $\sim$1.6 to 2 μm, which infers a surface roughness of $\frac{H}{\lambda} \simeq 0.2$ to 0.25. We approximate these microscale morphologies as one-dimensional surfaces that are periodic along the x-direction. We represent each surface within its period length λ with n two-noded elements, each element of uniform dimension, $dx = \frac{\lambda}{n}$ along the x-direction (Fig. 1b); the first ($i = 1$) and last nodes ($i = n + 1$) are tied together to enforce surface continuity across the periodic domain. (a) Incident xenon atoms (red arrows in Fig. 1) are introduced into the system at random positions above the carbon surface with assigned kinetic energy E_{Xe}, and are propagated along the assigned global ion incidence angle θ_{Xe} until the ion path intersects with a surface element, indicating a point of impact. (b) Since each element represents the homogenized response from MD [25], we compute the number of sputtered primary carbon atoms based on the steady-state sputtering yield data, Y_i, from MD (Fig. 1c), which is a function of both E_{Xe} and the local ion incidence angle $\overline{\theta}_{Xe}$ at the impact site [25]. For example, a sputter yield of 1.2 atoms/ion implies a 100 % probability of sputtering a first primary carbon atom and a 20 % probability of sputtering a second primary carbon atom from the impact site. (c) For each sputtered primary carbon atom (blue arrows, Fig. 1d), we also compute the corresponding energy E_C and trajectory, which are statistically selected based on the cumulative distribution functions of the sputtered carbon angles [25] and energies (see Table S1 and Fig. S1 of the Supplementary Materials) from prior MD simulations. (d) Tracing the trajectory of each of these primary carbon sputterants (blue arrows, Fig. 1b), we determine if they intersect another surface element or if they escape from the simulation box. (e) In the case of the former, we compute the probability of emission of secondary carbon sputterants from the impact site and sample the trajectories of these secondary sputterants (purple arrows, Fig. 1b) from a cosine distribution [27]. (f) Should these secondary carbon sputterants impact another surface element, we assume the sputterants to be absorbed at the impact site.

We remark that process (e) above necessitates new MD simulations to elucidate the sputtering yield of secondary carbon sputterants caused by the bombardment of primary carbon sputterants on amorphous carbon substrates. Following the same MD modeling approach as before [25], we subject an amorphous carbon substrate, created by the bombardment of xenon ions under steady-state sputtering conditions, to the bombardment of carbon atoms with incidence energies E_C of 1 to 150 eV and across local incidence angles α_C of $0^\circ, 30^\circ, 60^\circ, 75^\circ$. Note that this E_C range corresponds to the energy range reported for primary carbon sputterants (Fig. S1 of the Supplementary Materials). As shown in Fig. 1e, the primary carbon atoms (blue spheres along the blue trajectories) can recoil upon impact or can be deposited onto the surface; these processes can potentially trigger the release of secondary carbon sputterants (purple trajectories). For simplicity, we do not distinguish between these processes, and compute the probability of secondary sputterant emission as the ratio of carbon atoms exiting the MD simulation box (regardless of the carbon atom source) to the bombarded primary carbon sputterants. For each combination of E_C and α_C, we perform 30 individual bombardments and summarize our results in Table S2 of the Supplementary Materials. As expected, increasing E_C and α_C tends to increase the probability of secondary carbon sputterant emission.

To reduce computational effort and to allow for parallelization in our kinetic Monte Carlo simulations, we simultaneously deposit multiple xenon ions over the periodic surface length, λ, at each time instant with a fixed incremental fluence of $d\xi = 10^{14}$ $\left(\frac{\text{ions}}{\text{cm}^2}\right)$. We do not distinguish between the primary and secondary sputterants and compute the total number and trajectory of carbon atoms escaping from the simulation domain to obtain the average sputtering yield $\widehat{Y}$ (atoms/ion) and differential yield profile $f(\theta_C)$ at this fluence ξ. During each sputter or deposition event at the impact site of each element, we linearly interpolate the decrease or increase in the number of carbon atoms from the impact site to the corresponding nodes using linear finite element shape functions. The global sputtering yield $\widehat{Y}$ can also be obtained at the elemental level by summing the sputtering yield Y_i at each node

$$\widehat{Y} = \sum_{i=1}^{n} Y_i = \sum_{i=1}^{n} (S_i - D_i) \tag{1}$$

where S_i and D_i are the number of sputtered and deposited carbon atoms for node i, respectively, per incremental fluence $d\xi$ and λ. The deposition (sputtering) of a single carbon atom at the node increases (decreases) its height h_i by $(\rho\ dx)^{-1}$ where ρ is the atomic number density of the carbon surface material. After the dynamic stochastic processes have been resolved at each $d\xi$, we update the vertical height, h_i, of each node by

$$dh_i = \frac{(D_i - S_i)\lambda d\xi}{\rho dx} \tag{2}$$

to "evolve" the surface. The repeated ion bombardment creates a dual layer carbon structure, comprising of an amorphous subsurface layer (shaded gray in Fig. 1b) of atomic number density, $\rho = 0.8 \times 10^{23}$ atoms/cm^3, with thickness spanning the penetration depth ($\sim$3 nm) of the xenon ion, followed by the undamaged carbon substrate beneath [25]. We attain the same amorphous carbon structure regardless of the ion incidence energies and angles. The continued removal of carbon atoms from the amorphous layer by sputtering will allow xenon ions to

penetrate deeper into the substrate, effectively shifting this amorphous subsurface layer of constant thickness downwards. As such, ρ in (2) is effectively a constant.

In theory, we are free to select any element size dx in our Monte Carlo simulations. However, a large $\frac{dx}{\lambda}$ typically results in significant numerical errors because it cannot adequately represent an undulating surface geometry, while a small $\frac{dx}{\lambda}$ leads to physical traits that are more subtle. The underlying bases of our Monte Carlo simulations are the sputtering predictions (sputtering yield, differential yield profile, sputterant energy, etc.) where the sputtering characteristics of each element are homogenized from MD simulations, i.e., all the nanoscale sputtering mechanisms (ion-induced mass redistribution and viscous flow [30,50,52]) are averaged over a 5×5 nm^2 exposed surface area in MD [25]. As such, dx represents the characteristic length-scale of local surface features and it has to be several-folds larger than the size of the MD simulation box (~ 5 nm) used to obtain the steady-state sputtering yield response. AFM measurements of the surface height map of amorphous carbon films in Fig. 1a show the surfaces to have height variations (amplitude) of $\sim$200 nm, with peak-to-peak wavelength of $\lambda \simeq 1.6$ to 2 μm [22], which suggests $\frac{dx}{\lambda} \gg 0.0025$. Here, we adopt a fixed element size of $\frac{dx}{\lambda} = 0.01$ (i.e., $dx = 20$ nm for $\lambda = 2$ μm) in our Monte Carlo simulations. Regardless, our numerical studies further show that the choice of $\frac{dx}{\lambda}$, at least within the bounds of 0.0025 and 0.025, does not significantly change the overall surface topology evolution (see Fig. S2 of the Supplementary Materials).

In our Monte Carlo simulations, we do not consider the impact of recoiling xenon ions with surface features. Our prior MD simulations show that majority of the incident xenon ions are embedded within the carbon substrate at depths of 1 to 3 nm [25]. While some of these entrapped xenon ions may diffuse out of the substrate, they do so at relatively low energies and cannot induce any further breaking of carbon-carbon bonds. We also do not consider the effects of surface reconstruction or carbon atom diffusion in our Monte Carlo simulations. We have performed MD simulations where we subject the amorphous carbon structure from xenon ion bombardment to elevated temperatures of $\sim$2000 K, maintained by a Berendsen thermostat for 10 ns. We observe negligible movement or reconfiguration of carbon atoms, which confirms the slow thermal-induced diffusion characteristics expected of a covalently-bonded system.

3. Surface evolution mechanism

We elucidate the general mechanisms of sputtering for a periodic undulating surface idealized by an initial sinusoidal topology along the x-direction

$$h(x) = \frac{H}{2}\left[1 - \cos\left(\frac{2\pi x}{\lambda}\right)\right] \tag{3}$$

where $\frac{H}{2}$ denotes the amplitude, and the surface roughness can be quantified by the normalized parameter $\frac{H}{\lambda}$. Motivated by AFM surface roughness measurements of amorphous carbon films [22], we adopt $\frac{H}{\lambda} = 0.25$ as our initial configuration, and quantify the morphology evolution as a function of xenon ion fluence ξ for a fixed ion energy of $E_{Xe} = 500$ eV under normal and oblique ion incidence angles ($\theta_{Xe} = 0°, 60°$).

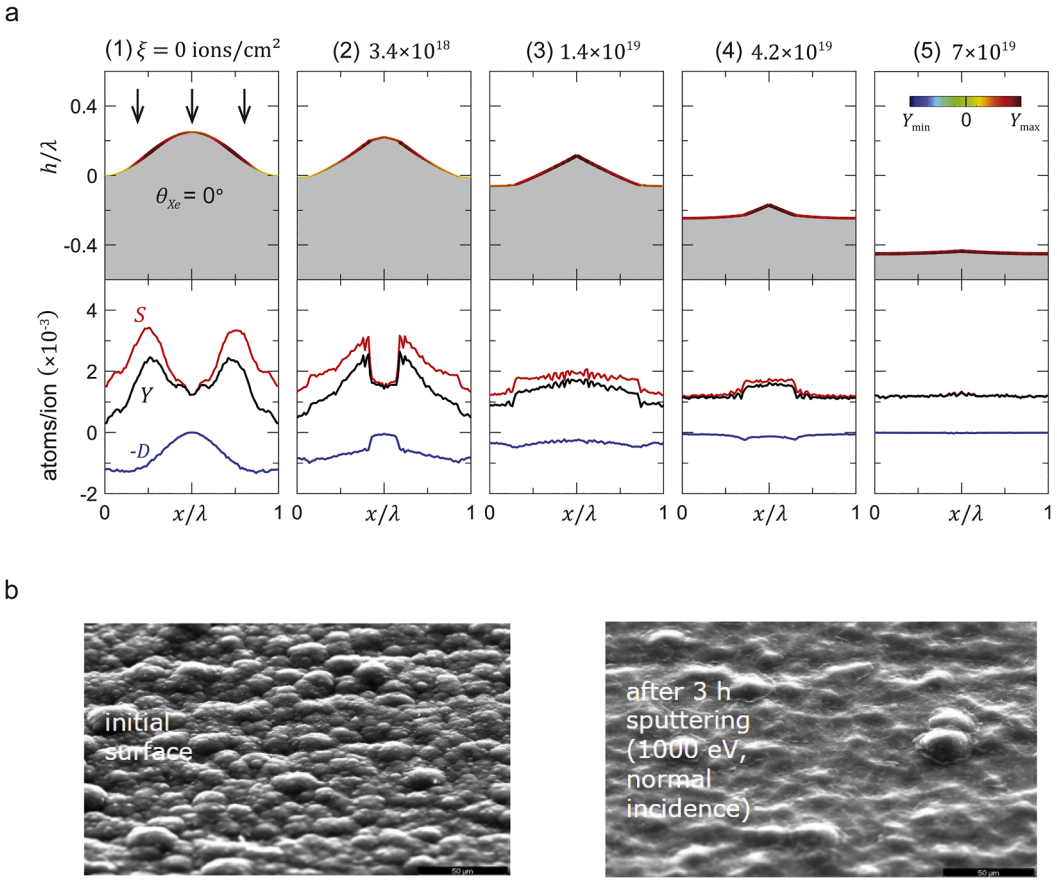

Fig. 2. **(a)** Sputtering of an initial sinusoidal surface with $\frac{H}{\lambda} = 0.25$ under an ion fluence with $E_{Xe} = 500$ eV, $\theta_{Xe} = 0°$. Top: morphology evolution with ion fluence ξ; surface contours delineate elements with high yields of deposited atoms (Y_{min}) and sputterants (Y_{max}), respectively. Bottom: spatial distributions of the elemental yields of sputterants S and deposited atoms D, and elemental sputtering yields $Y = S - D$. **(b)** SEM imaging of pyrolytic graphite before and after three hours of sputtering with $E_{Xe} = 1$ keV, $\theta_{Xe} = 0°$, depicting distinct surface smoothening [18].

We have also repeated our simulations under different ion energies ($E_{Xe} = 200,\ 1000$ eV) and incidence angles ($\theta_{Xe} = 0°, 30°, 60°$) and have observed similar morphological transitions (Figs. S3 and S4 of the Supplementary Materials).

3.1. Normal ion incidence

Fig. 2a-top shows the evolving surface configurations 1 to 5 under a normal ion incidence. We color the surface to denote the expected elemental sputter yield $Y(x) = S(x) - D(x)$ obtained by freezing the current surface to compute with Monte Carlo the average yield of sputterants S and deposited atoms D for each element over a large ion fluence to ensure statistical independence; we depict the spatial distribution of these quantities in Fig. 2a-bottom. For the initial geometry (Fig. 2a-1), the locations with the highest erosion ($Y_{\max}$) coincide with $\frac{x}{\lambda} = 0.25,\ 0.75$ where the local ion incidence $\overline{\theta}_{Xe}$ is the highest ($\sim 75°$). Comparatively, the crest and trough ($\overline{\theta}_{Xe} \simeq 0°$) have much lower Y, particularly at the trough where $Y_{\min}$ is observed because of the confined geometry which promotes sputterant redeposition (higher D), versus the unobstructed geometry of the crest where $D \simeq 0$.

The accelerated erosion at local regimes with high $\overline{\theta}_{Xe}$ results in tapering and sharpening of the crest along with flattening of the trough (Fig. 2a-2). A symmetrical bilinear surface structure with bilinear distributions of S, D, and Y, now develops: a perfectly flat, low erosion, regime centered at the former trough, transitioning to an inclined, higher erosion, regime with a constant slope, which peaks at the former crest (Fig. 2a-3). In the absence of substantial variations in D, a flat regime will always remain flat under a normal ion incidence. Continued sputtering therefore causes the self-similar size reduction of this triangular protrusion (Fig. 2a-4), and a microscopically flat surface is eventually obtained (Fig. 2a-5). This flattening of surface features after long time exposure to xenon ions has been reported experimentally, as shown by SEM images in Fig. 2b for the sputtering of pyrolytic graphite under a normal xenon incidence ion with energy of 1 keV [18].

3.2. Oblique ion incidence

The sputtering process becomes more complicated under a highly oblique ion incidence, triggering multiple erosion and deposition mechanisms at three distinct length-scales depicted in Fig. 3. This is in part because of the activation of surface shielding effects which are absent under a normal ion incidence. At the length-scale spanning several elements, the competing sputtering (red arrows) and sputter deposition process (blue arrows) can introduce small variations in the local yield, which increases the local surface (elemental) undulations (Fig. 3a). Relative to the back-faces of these elemental undulations that are (partially) shielded from the incoming ions, the ion-facing sides are subjected to high ion fluxes but can also trap a considerable amount of sputtered carbon species. The elemental undulations are smoothened to recover a flattened surface when sputtering effects are dominant but grow into a more distinctive microscale surface feature spanning multiple (10 or more) elements when deposition effects are dominant (Fig. 3a). The latter results in roughening of the overall surface topography at the microscale.

The competing sputtering and sputter-deposition mechanisms, resulting in roughening and smoothening and the eventual development of distinctive morphology changes at the microscale, are observed in our Monte Carlo simulations for $\theta_{Xe} = 60°$ in Fig. 4a (see also Movie S1 of the Supplementary Materials). Because the maximum sputtering yield is attained at $\overline{\theta}_{Xe} \simeq 75°$, sputter erosion is concentrated at the crest of the sinusoidal morphology (Fig. 4a-1), leading to flattening of the peak (Fig. 4a-2). In the process, a small undulation now develops at 'A' in Fig. 4a-2, with high and low sputtering rates on the ion- and back-facing sides of this undulation, but this peak is eventually flattened with continued bombardment (Fig. 4a-3). However, three other new undulations develop at 'B', 'C', and 'D' in Fig. 4a-3, and eventually grow

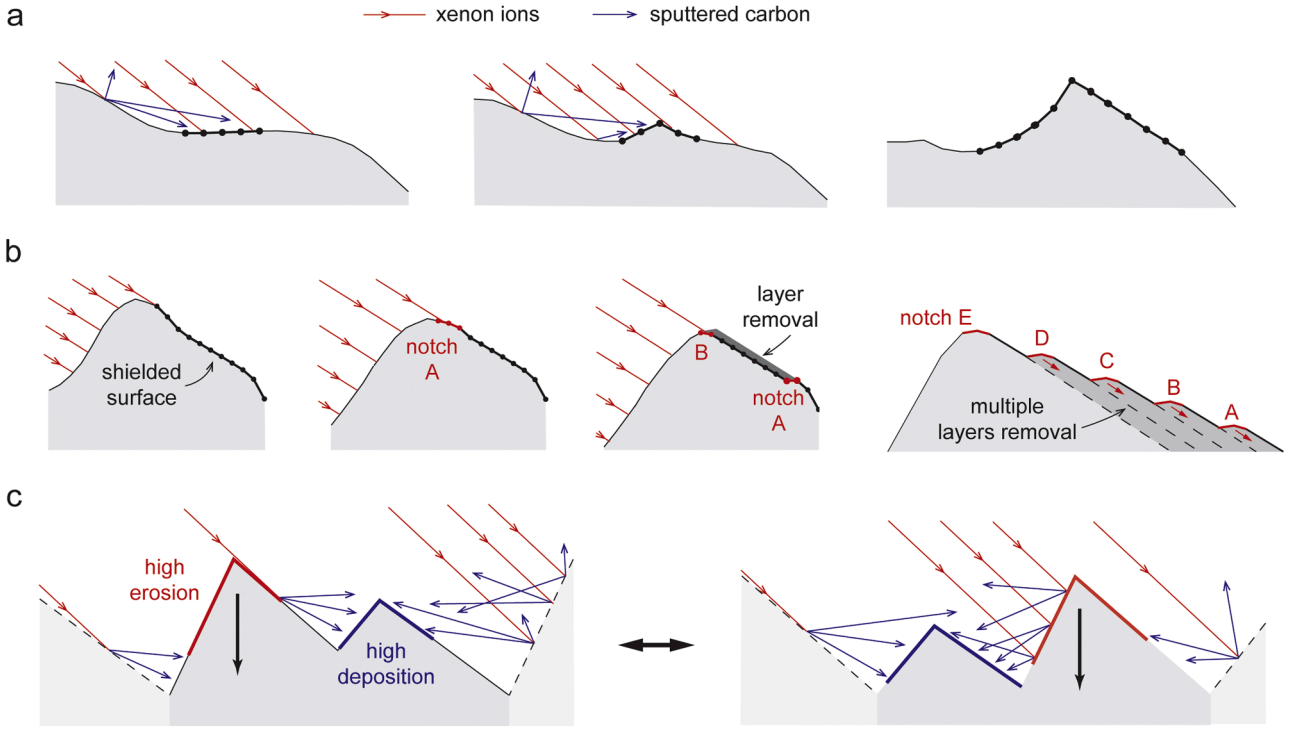

Fig. 3. Overview of the multiscale sputter-erosion mechanisms of an undulating surface under an oblique ion fluence, caused by competing sputter erosion (red) and sputter deposition (blue) processes. **(a)** Nucleation of elemental undulations to form microscale undulations spanning multiple surface elements. **(b)** Erosion of microscale undulations to form surface steps, with the ion- and back-facing surfaces oriented perpendicular and parallel to the beam direction; concentration of sputtering at the notch-tips results in simultaneous layer-by-layer erosion on the back-faces. **(c)** Concomitant decay of neighboring surface steps, resulting from the alternating and fluctuating deposition versus sputtering rates among these surface steps.

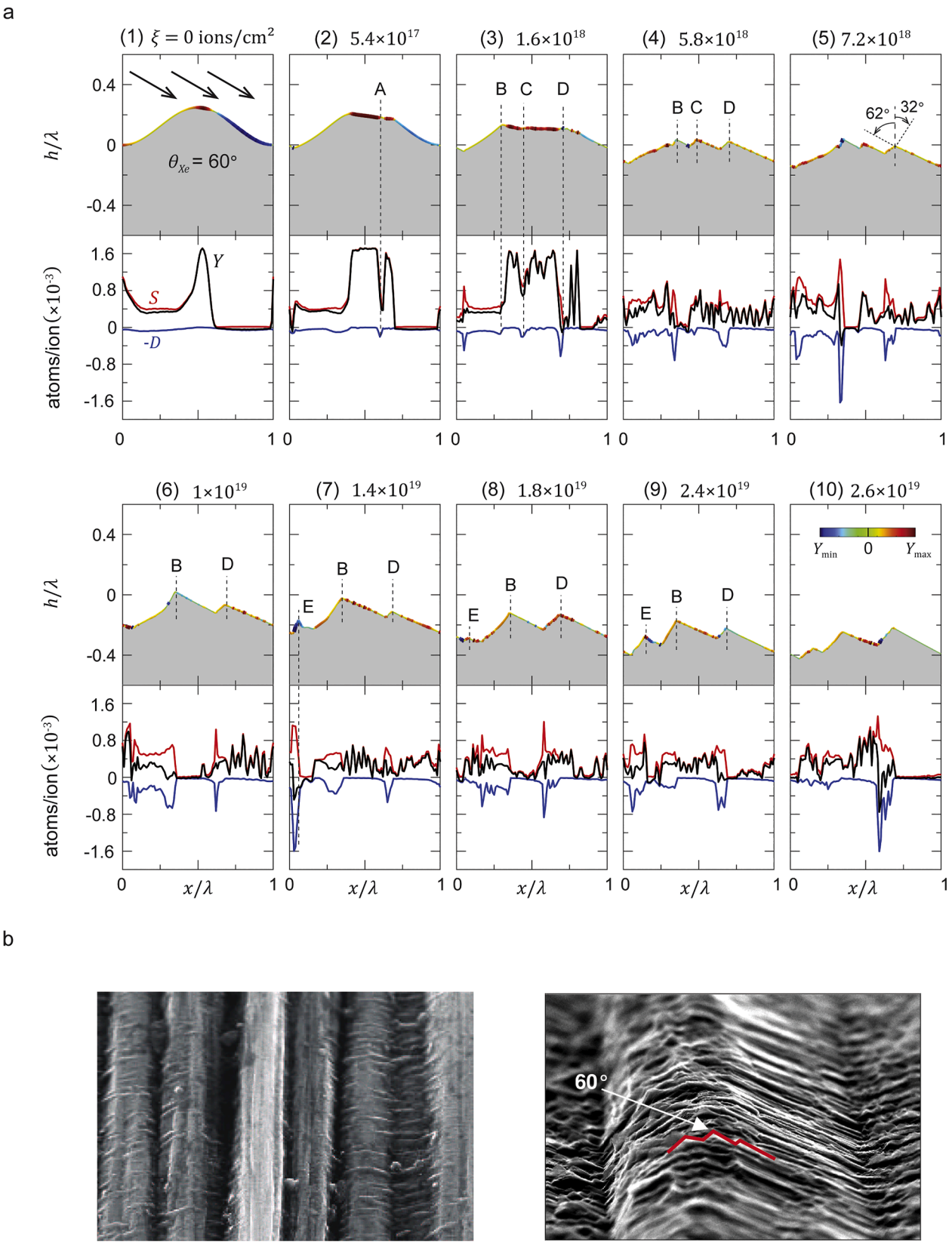

Fig. 4. **(a)** Sputtering of an initial sinusoidal surface with $\frac{H}{\lambda} = 0.25$ under an ion fluence with $E_{Xe} = 500$ eV, $\theta_{Xe} = 60^{\circ}$ Top: morphology evolution with ion fluence ξ; surface contours delineate elements with high yields of deposited atoms ($Y_{\min}$) and sputterants ($Y_{\max}$), respectively. Bottom: spatial distributions of the elemental yields of sputterants S and deposited atoms D, and elemental sputtering yields $Y = S - D$. **(b)** SEM imaging of an exposed carbon fiber before and after four hours of sputtering with $E_{Xe} = 500$ eV, $\theta_{Xe} = 60^{\circ}$, depicting the formation of surface steps [17].

into distinctive microscale undulations (Fig. 4a-4), which span over half of the simulation domain.

All these microscale undulations have a common characteristic: the ion- and back-facing sides are roughly normal and parallel to the incidence ion flux, respectively, to resemble surface steps (see Fig. 4a-5). The flattening of the ion-facing surface to attain $\overline{\theta}_{Xe} \simeq 0^{\circ}$ is akin to the morphology transitions from a rough to uniformly flat surface under a normal ion incidence (Section 3.1), and the ion-facing surface remains flat barring significant sputterant deposition. On the back-faces, any elemental undulations are rapidly eroded by the ion flux to create a flat, parallel surface that is shielded from the incidence ions by the tip of the surface steps, as illustrated in Fig. 3b. However, the high curvature at the tip facilitates rapid erosion to form a notch in the back-face, which propagates downhill with subsequent ion erosion. In turn, the nucleation and propagation of new notches lead to simultaneous removal of multiple layers of material on the back-face of each surface step. The erosion fronts (notches) of these material layers are characterized by intense but localized sputtering, as shown by the multiple dark red spots in the surface morphology contours (top), accompanied by rapid fluctuations in the sputtering signatures (bottom) on the back-faces of surface steps 'B', 'C', 'D', and 'E' in Fig. 4a-4 to 4a-10. Similar microscale surface step features have been observed in the sputtering of exposed carbon fiber in carbon-carbon composites under the same xenon ion bombardment conditions of $E_{Xe} = 500$ eV, $\theta_{Xe} = 60^{\circ}$, as shown by SEM images in Fig. 4b [17].

We remark that sputter erosion of these microscale surface steps does not occur in isolation. As illustrated in Fig. 3c, when a surface step is neighboring to, or sandwiched between, higher surface step(s), the deposition of sputterants from the neighboring surface step(s) could offset its own sputter erosion and forestall its decay. Once the neighboring surface step(s) is now eroded to below a critical height, the reverse occurs where the decay of the neighboring surface step(s) is now forestalled at the expense of the now-taller surface step. This process allows for the concomitant decay of two or more surface steps and is the mechanism underpinning the alternate and fluctuating decay rates among the surface steps 'B', 'D', and 'E' in Fig. 4a-7 to 4a-10.

4. Transient to steady-state sputtering yield

The morphology evolution under xenon ion fluence (ξ) is accompanied by changes to the global sputtering yield ($\widehat{Y}$), as shown in Fig. 5 for $E_{Xe} = 500$ eV with $\theta_{Xe} = 0^{\circ}, 30^{\circ}, 60^{\circ}$. Under a normal ion fluence ($\theta_{Xe} = 0^{\circ}$), the sputter yield monotonically decreases with ξ following the transition from a sinusoidal morphology to a sharp triangular morphology, and the subsequent self-similar erosion of this triangular protrusion. Beyond a fluence of ξ_{ss}, steady-state sputtering yield is reached as a microscopically flat surface morphology is maintained. Under oblique incidence angles, highly oscillating sputtering yields, particularly for $\theta_{Xe} = 60^{\circ}$, are observed during the transient phase due to competing and evolving smoothening and roughening mechanisms at both the elemental- and micro-scales, resulting in the formation of surface steps (Section 3.2). Even beyond the steady-state fluence ξ_{ss} (operationally defined as a regime where the local variation in the sputtering yield $\Delta\widehat{Y} \leq 10$ %), the concomitant interaction, resulting in the alternating decay of neighboring surface steps at the mesoscale, leads to a fluctuating steady-state sputtering yield.

We summarize the above transitions and fluctuations in the sputtering yield with a box and whisker plot (inset in Fig. 5). Here, we use the whisker limits (a,e) to represent the maximum and minimum $\widehat{Y}$ across the entire range of ξ, while the three box markers (b,c,d) are taken to represent the maximum, mean, and minimum values of $\widehat{Y}$ beyond ξ_{ss}. Fig. 6 compares our Monte Carlo sputtering yield predictions (blue box and whisker plots) across E_{Xe} of 200 to 1500 eV with $\theta_{Xe} = 0^{\circ}, 30^{\circ}, 60^{\circ}$, against prior MD simulations [25] (red symbols) and existing sputtering yield measurements for various allotropes of carbon (black symbols)

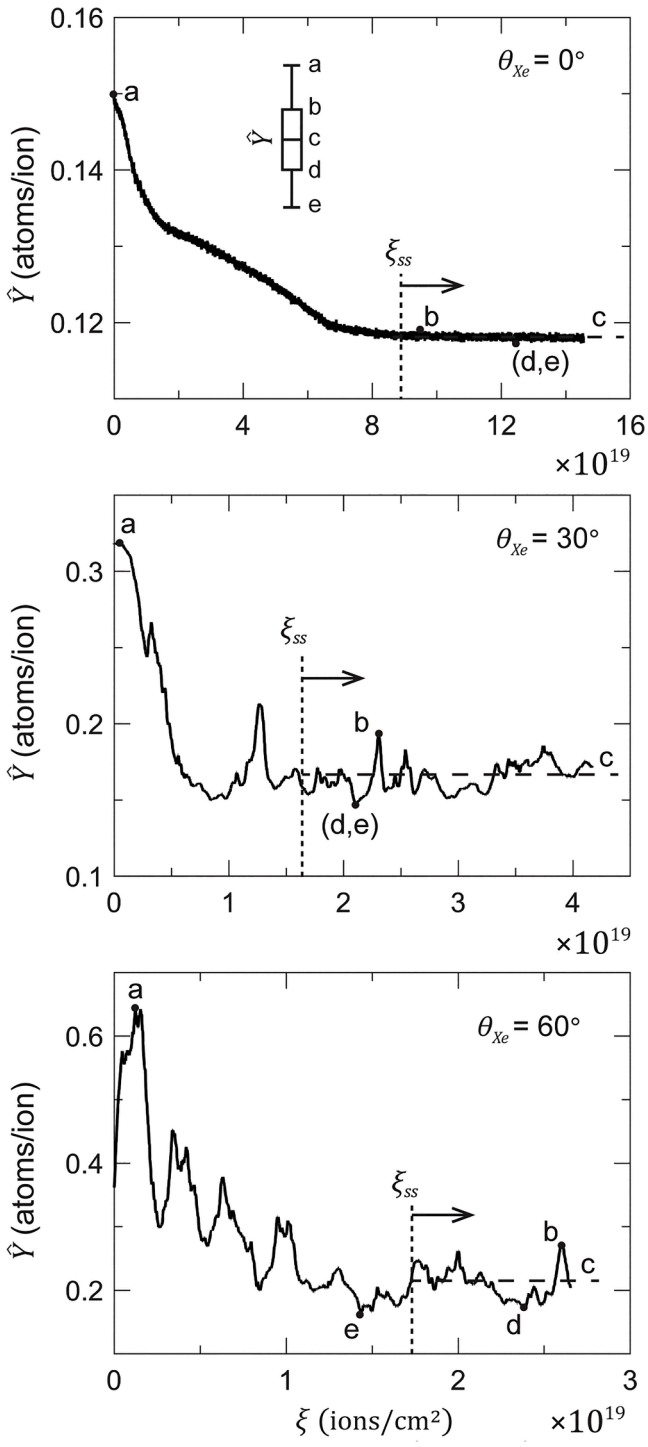

Fig. 5. Evolution of the sputtering yield ($\widehat{Y}$) with ion fluence (ξ) under $E_{Xe} = 500$ eV, $\theta_{Xe} = 0^{\circ}, 30^{\circ}, 60^{\circ}$. Inset: box and whisker plot summarizing fluctuations in $\widehat{Y}$ within the transient ($\xi < \xi_{ss}$) and steady-state ($\xi > \xi_{ss}$) regimes; whisker limits (a,e): maximum and minimum $\widehat{Y}$ across the entire ξ; box markers (b,c,d): maximum, mean, and minimum $\widehat{Y}$ within $\xi > \xi_{ss}$.

[17–24]. Under a normal ion incidence, the consistently smooth transition of $\widehat{Y}$ to its steady-state value infers that (b,c,d,e) in each box and whisker plot collapses to a single point representing the lower limit of $\widehat{Y}$. Across all ion energies, this lower limit coincides with the sputtering yield predictions from MD since we ultimately attain a uniformly flat surface at steady-state, while the upper whisker limits represent the

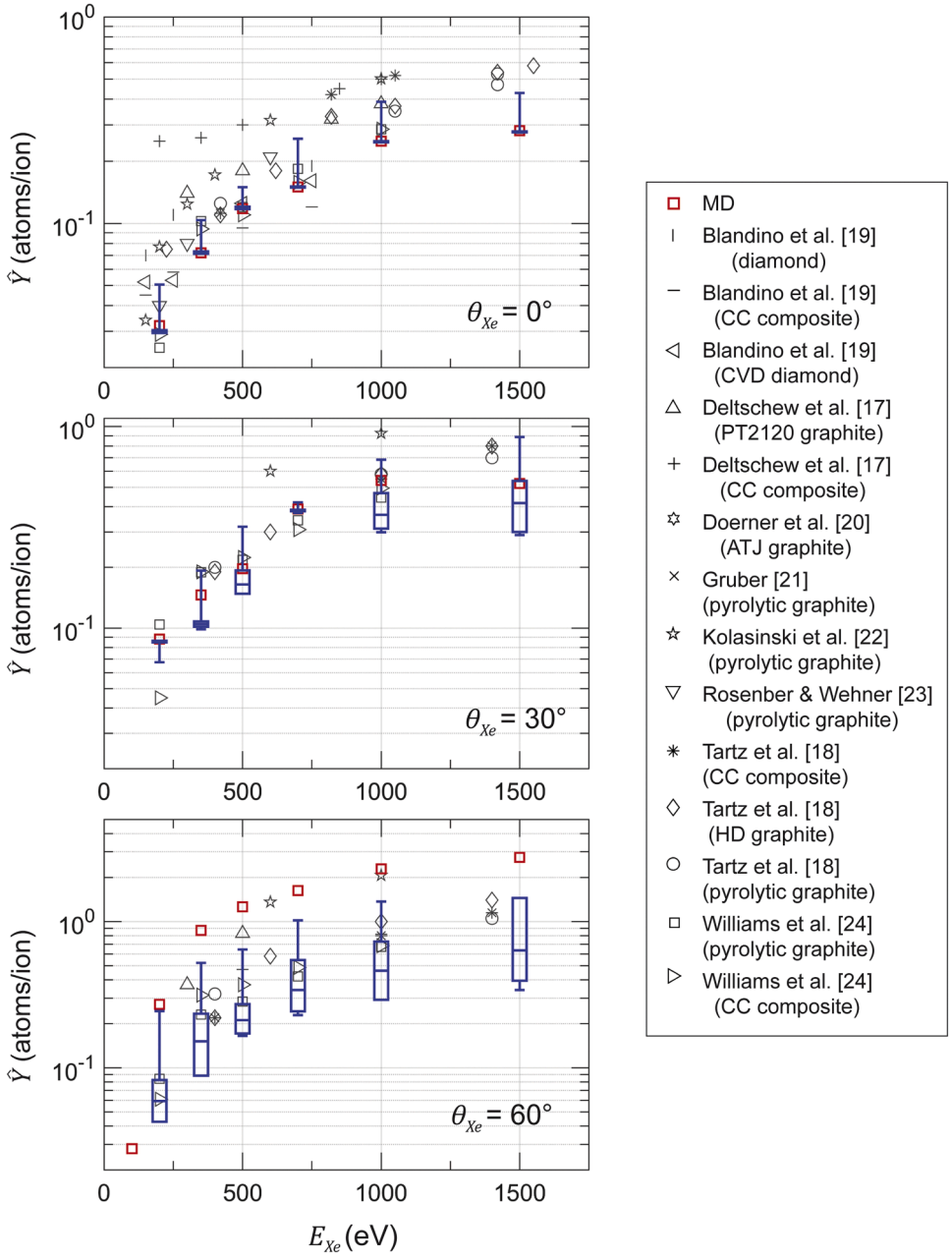

Fig. 6. Comparison of sputtering yield ($\hat{Y}$) predictions from Monte Carlo simulations (blue box and whisker plots) versus MD simulations (red squares) and sputtering experiments (black symbols), across various E_{Xe} and θ_{Xe}.

initial sputtering yields of the assumed sinusoidal morphologies with $\frac{H}{\lambda} = 0.25$. The box and whisker representations become more distinctive under an oblique ion fluence because of the increased scatter in $\hat{Y}$. The steady-state sputtering yield predictions now differ significantly from MD predictions because of the formation of characteristic surface steps. In particular, MD predictions are now outside the whisker limits of the Monte Carlo simulations for $\theta_{Xe} = 60^{\circ}$ because of this increased surface roughness.

The sputtering yield is highly dependent on the evolving surface morphology within the transient regime, and an accurate and consistent measurement of the sputtering yield can only be established within the steady-state regime. This presents a challenge to experimental measurements of the sputtering yield, since one cannot ascertain the value of ξ_{ss} a-priori. The upper and lower whisker limits from our Monte Carlo simulations in Fig. 6 define the bounds of the expected sputtering yield (albeit within the assumption of an initial sinusoidal morphology), with the steady-state values (box markers) constituting the lower end of the experimental measurements. Our computations show that ξ_{ss} is at least several-folds higher for $\theta_{Xe} = 0^{\circ}$ than for $\theta_{Xe} = 30^{\circ}, 60^{\circ}$ (Fig. S5 of the Supplementary Materials), which could explain the closer proximity of the experimental measurements to the upper whisker limits for the former. Nevertheless, most of the experimental scatter across the range of E_{Xe} and θ_{Xe} are well-contained within the whisker limits. Notably, the box plots depicting sputter yield variations at steady-state encompass nearly all of the experimental data by Williams et al. [24], which utilizes a more accurate method of quartz crystal microbalance (QCM) [26,53,54] to measure the steady-state sputtering yield versus conventional mass loss measurements.

To elucidate the sensitivity of the differential sputter yield profile to the evolving surface morphology with ion fluence, we show in Fig. 7 the probability density function (PDF) of the angular distributions of carbon

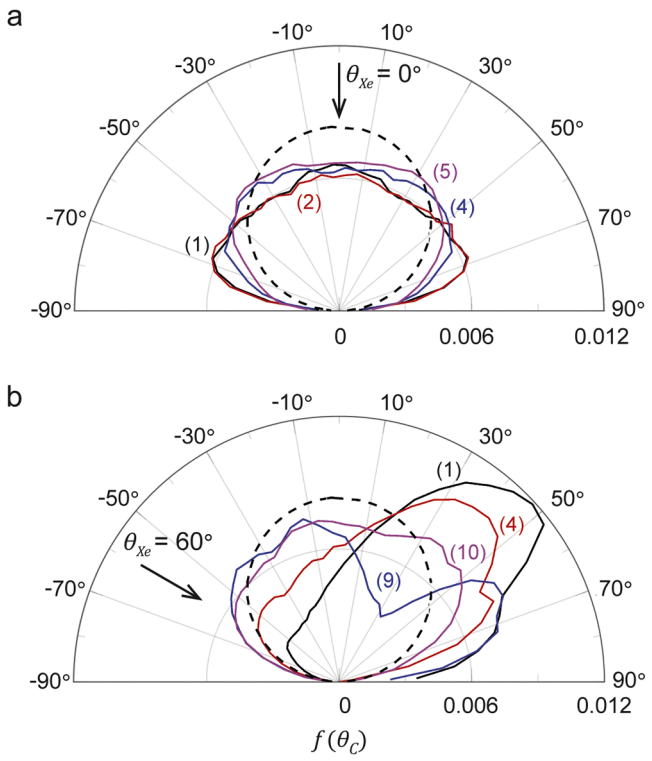

Fig. 7. Probability density function (PDF) of the differential yield profiles of carbon sputterants for $E_{Xe} = 500$ eV, $\theta_{Xe} = 0°, 60°$ Each (x) in (**a**) and (**b**) corresponds to the respective surface morphologies at various ξ in Figs. 2a-x and 4a-x, respectively. Dashed curves denote the PDF of the cosine angle distribution [27].

sputterants, $f(\theta_C)$, for $E_{Xe} = 500$ eV and $\theta_{Xe} = 0°, 60°$, at various ξ with '(x)' corresponding to the respective topographies in Figs. 2a- and 4a-x. No significant change to the differential profile is observed under a normal ion incidence angle. Under an oblique ion incidence of $\theta_{Xe} = 60°$, however, the differential yield distinctly favors the front-scatter direction (50° to 60°) for the initial sinusoidal morphology, but increasing amount of backward scatter is observed with the development of surface steps, and $f(\theta_C)$ transitions closer to a cosine angle distribution (dashed curve) [27] at steady-state. In fact, the differential yield alternates between the blue and purple profiles corresponding to Fig. 4a-9 and 4a-10 at steady-state due to the alternating decay of neighboring surface steps. Similar relationships between the evolving surface morphology and differential yields are observed at $E_{Xe} = 200$ eV and 1 keV (Figs. S6 and S7 of the Supplementary Materials).

5. Sputtering-by-design

We expand our studies to include the effects of varying initial surface morphologies to gain insights into design strategies for controlling the sputtering yield. Our earlier analyses are based on an initial sinusoidal morphology with $\frac{H}{\lambda} = 0.25$. Fig. 8 examines the effects of $\frac{H}{\lambda}$ on the morphology evolution and the sputtering yield for $E_{Xe} = 500$ eV with $\theta_{Xe} = 0°, 30°, 60°$ When the surface is sufficiently rough $\left(\frac{H}{\lambda} \geq 0.2\right)$, the surface morphologies at steady-state (colored curves in Fig. 8a) are virtually independent of the initial topology (black curves in Fig. 8a): we obtain a uniformly flat surface at $\theta_{Xe} = 0°$, and characteristic surface steps at $\theta_{Xe} = 30°$ and 60°. For a sufficiently smooth initial surface ($\frac{H}{\lambda} = 0.1$), elemental undulations cannot develop if the sputtering yield is nearly spatially homogeneous under $\theta_{Xe} = 30°$. Meanwhile, multiple elemental undulations can still develop under a high ion incidence angle of $\theta_{Xe} = 60°$, giving rise to the formation of multiple, albeit smaller-dimension, surface steps at steady-state. The transition from a nearly-flat, smooth morphology to the development of these multiple surface steps is responsible for the significant reduction in the sputtering yield during the transition to reach steady-state (whisker height). As shown in Fig. 8b, increasing $\frac{H}{\lambda}$ dramatically reduces the initial sputter yield since the increasingly rough initial surface allows the ions to impact the surface at low local incidence angles. The opposite trend is observed for $\theta_{Xe} = 0°$, where the lowest sputtering yield is attained for a flat morphology; increasing $\frac{H}{\lambda}$ increases the initial sputtering yield, and consequently, the whisker height. Nevertheless, with the exception for $\frac{H}{\lambda} = 0.1$, $\theta_{Xe} = 30°$, the steady-state sputtering yield (box plots) is virtually independent of $\frac{H}{\lambda}$ since morphologically similar structures are eventually obtained.

We next examine the surface morphology and sputtering yield evolutions for a large variety of initial surface structures, beyond the

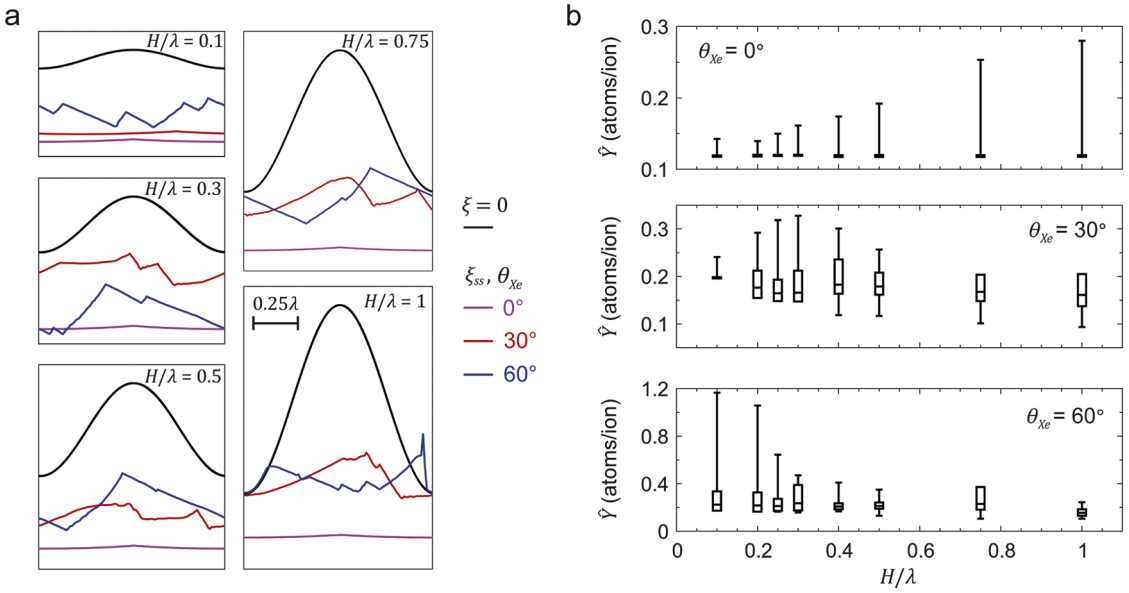

Fig. 8. Effects of initial surface roughness $\frac{H}{\lambda}$ under $E_{Xe} = 500$ eV, $\theta_{Xe} = 0°, 30°, 60°$ (**a**) Surface morphology evolutions at steady-state sputtering (colored curves), $\xi = \xi_{ss}$, from the initial sinusoidal morphologies at $\xi = 0$ (black curves). (**b**) Box and whisker summary of the sputtering yields ($\hat{Y}$).

idealized sinusoidal morphologies above. Under a normal ion incidence in Fig. 9 (also see Movie S2 of the Supplementary Materials), all but two of these structures evolve towards a morphologically flat surface and attain the same steady-state sputtering yield (Fig. 9a-f and Fig. 9h). The transient response of these structures, however, are sensitive to the initial morphology and can have transient sputtering yields that are higher or lower than the steady-state values. The sputtering yield of a surface represented by a periodic step function (Fig. 9g) is one interesting exception: both the morphology and the sputtering yield are almost unchanged across the range of ion fluence because the majority of the ions are already impacting the surface in the normal direction ($\theta_{Xe} \approx \overline{\theta}_{Xe} \approx 0^{\circ}$) from the start. Another exception is the semi-circular morphology (Fig. 9i), where the close periodicity leads to significant redeposition of the sputterants and drives the growth of thin vertical walls. These walls in turn are able to trap even more sputterants, significantly reducing the sputtering yield. Such vertical thin wall morphologies have been observed in the post-sputtered scanning microscopy images of exposed semi-circular carbon fibers subjected to similar ion conditions of $E_{Xe} = 500$ eV and $\theta_{Xe} = 0^{\circ}$ [17], as well as $E_{Xe} = 1$ keV and $\theta_{Xe} = 0^{\circ}$ [18]. Our simulations show that such wall structures cannot form when the periodic semi-circular morphologies are sufficiently far apart to reduce the contributions of sputter deposition (Fig. 9h).

Under an oblique ion incidence angle ($\theta_{Xe} = 60^{\circ}$), all of the surfaces evolve to form surface steps at steady-state, with similar steady-state sputtering yields of ~0.2 atoms/ion (Fig. 10; Movie S3 of the Supplementary Materials). The details of the initial morphology, however, are observed to control the eventual size-scales of these surface steps at steady-state. Interestingly, steep wall initial configurations in Fig. 10d,e,g result in the development of unique tapering thin wall structures (configuration 2) which momentarily reduces the sputtering yield to ~0.15 atoms/ion because of increased redeposition of the sputterants; the eventual erosion of these wall structures increases the sputtering yield back to its steady-state value.

Motivated by the above observations, we test the efficacy of two possible thin wall configurations, comprising of periodic near-vertical walls with a thickness to height aspect ratio of 1:5, in mitigating sputtering under $E_{Xe} = 500$ eV and $\theta_{Xe} = 0^{\circ}, 60^{\circ}$ (Fig. 11). Under $\theta_{Xe} = 0^{\circ}$, the steady-state sputtering yield of this wall configuration (solid line in Fig. 11a) is remarkably reduced by nearly 40 % compared to an initial sinusoidal morphology (black dash line) and is consistently lower than all of the prior experimental sputtering yield measurements ($\widehat{Y}$ values denoted by arrows). More importantly, the wall morphology is not significantly degraded by the sputtering process (Fig. 11a-1 to 11a-3)

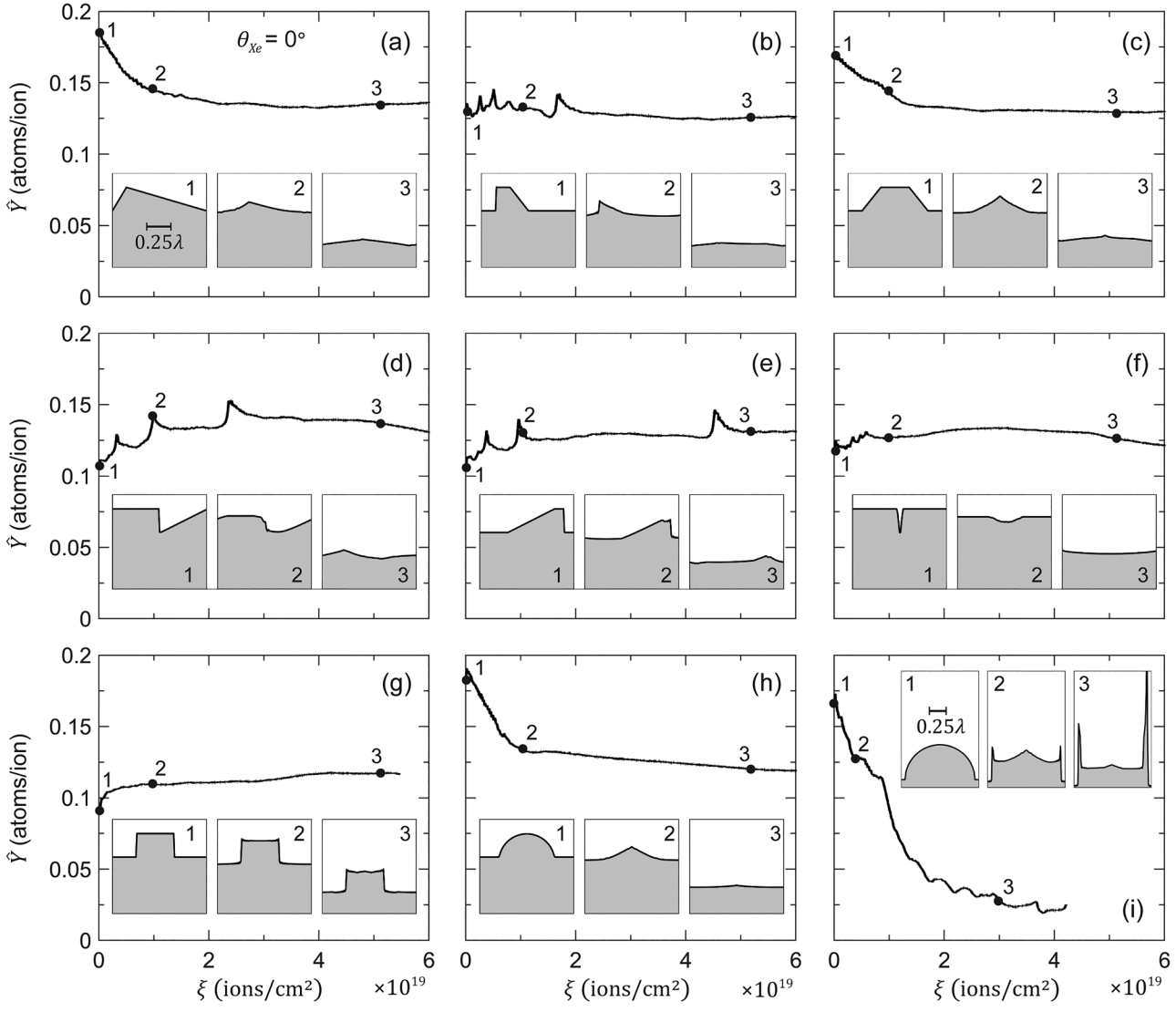

Fig. 9. Transient to steady-state evolution of the sputtering yield ($\widehat{Y}$) under $E_{Xe} = 500$ eV, $\theta_{Xe} = 0^{\circ}$ for different initial surface morphologies, with snapshots of the evolving morphologies.

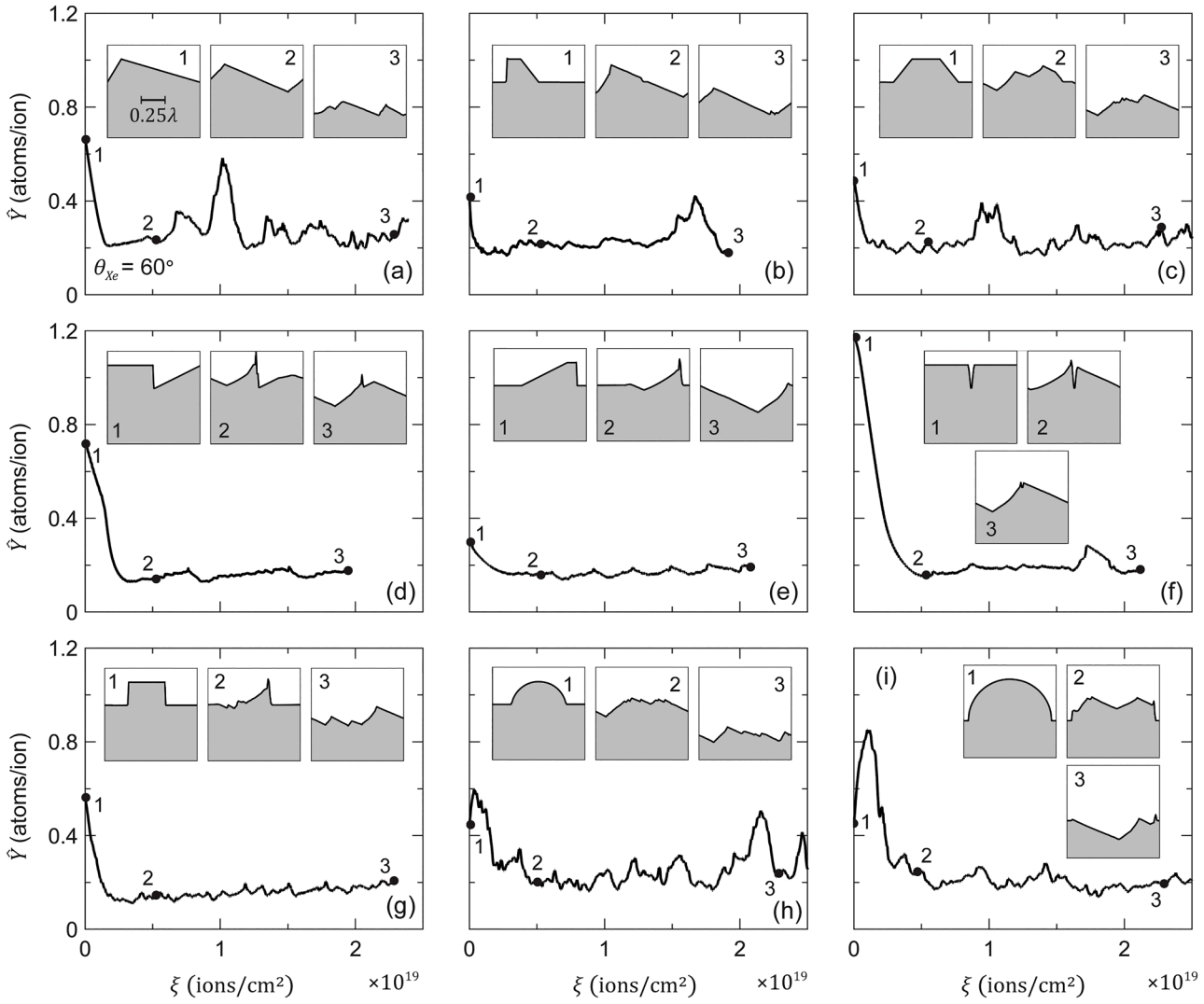

Fig. 10. Transient to steady-state evolution of the sputtering yield ($\hat{Y}$) under $E_{Xe} = 500$ eV, $\theta_{Xe} = 60^{\circ}$ for different initial surface morphologies, with snapshots of the evolving morphologies.

even at a very high fluence. Under $\theta_{Xe} = 60^{\circ}$, we have reduced the interval between each vertical wall to allow the ions to only impact the sacrificial wall structures, while allowing for significant re-deposition of the sputtered species (Fig. 11b). The bombardment process morphs the top-exposed surface of the vertical walls into sharp vertical peaks (akin to Fig. 10d,e,g) and dramatically reduces the sputtering yield to 0.1 atoms/ion. Surprisingly, this low sputtering yield can be sustained for a considerable amount of fluence, until the wall is completely degraded, giving way to formation of the usual characteristic surface steps at steady-state. We remark that this transient period of low sputtering yield can be extended with taller wall structures, since they act as sacrificial elements to delay the formation of surface steps.

6. Discussions and conclusion

Experiments have reported a large spread in the sputtering yield measurements of carbon under the bombardment of heavy ions, but could not establish a correlation between the sputtering yield and the various polymorphs and allotropes of carbon (e.g. graphite, diamond, carbon-carbon composites) [18,24]. Recent MD simulations [25] show that repeated bombardment of ions creates an amorphous carbon subsurface structure, that is largely independent of the ion energy and incidence angle, as well as the initial carbon structure. Thus, the sputtering yield at "steady-state" is expected to be independent of both the initial carbon structure as well as the prior sputtering history. From the standpoint of MD simulations, "steady-state" sputtering yield is attained once the initial carbon structure (graphite, diamond) has been transformed to this unique amorphous carbon subsurface structure. However, this microstructural transformation requires an ion fluence that is several-orders-of-magnitude smaller compared to that required to evolve a surface to attain its steady-state morphology in our Monte Carlo simulations. Starting from a multilayer graphitic structure, for example, MD simulations require an ion fluence of $\sim 10^{15}$ ions/cm^2 to attain its amorphous subsurface structure [25], versus 10^{19} to 10^{20} ions/cm^2 for the range of initial morphologies considered here to transition to the steady-state characteristic structures. Thus, this surface morphological transition is the limiting time-scale to achieve true steady-state sputtering yield.

Regardless of the initial surface morphology (with exception of specifically designed stepped structures), we show that a normal ion flux always erodes a morphologically rough surface to become uniformly flat to achieve steady-state sputtering yield. Similarly, a high oblique ion flux always creates characteristic surface steps at steady-state through a multiscale process involving: (a) the nucleation of local surface (elemental) undulations, which grow to form microscale surface steps, (b) layer-by-layer slicing of these surface steps, and (c) concomitant

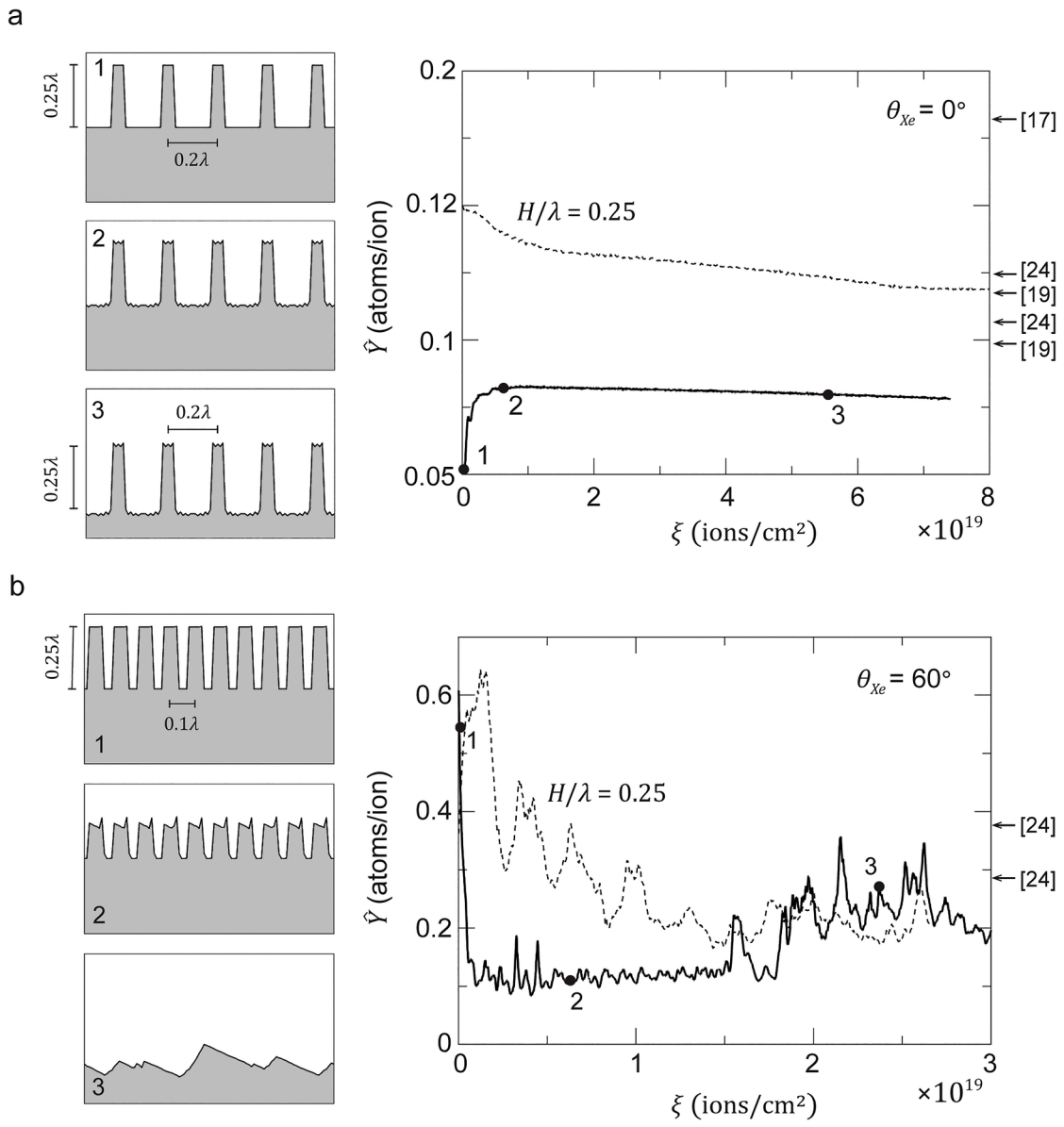

Fig. 11. Periodic, near-vertical, wall structures to forestall sputtering under $E_{Xe} = 500$ eV with $\theta_{Xe} = 0^{\circ}$ (**a**) and $\theta_{Xe} = 60^{\circ}$ (**b**). Left: snapshots of the evolving surface morphologies. Right: evolution of the sputtering yield ($\widehat{Y}$) for the proposed wall structures (solid curves) versus an initial sinusoidal morphology with $\frac{H}{\lambda} = 0.25$ (dashed curves); black arrows: experimental sputtering yield measurements from literature.

alternating decay of neighboring steps. At moderate ion incidence angles, the steady-state sputtering configurations can transition to either of these two surface structures (flat versus surface steps), depending on the roughness of the starting morphologies and the incidence xenon energy. Consequently, while one cannot expect the initial surface morphologies of different carbon structures used in various sputtering experiments to be even remotely similar, our studies here suggest that the steady-state sputtering yield is not very sensitive to the initial surface morphology.

Our Monte Carlo simulation results are in good agreement with prior sputtering experiments. Under a normal xenon ion flux with energy of 1 keV, SEM images show distinct smoothening of the morphologies across all carbon surfaces (including polished and unpolished pyrolytic graphite, graphite with different grain sizes, and carbon-carbon composites) after 3 h of sputtering, regardless of the initial surface roughness (Fig. 2b) [18]. Under an oblique ion flux ($\theta_{Xe} = 60^{\circ}$), SEM imaging shows the initial cylindrical morphologies of exposed carbon fibers (resembling the initial morphologies in Fig. 10h,i) erode to form microscale surface steps, with characteristic features which are virtually identical to those observed in our simulations [17], i.e. ion- and back-facing sides of each step are approximately perpendicular and parallel to the beam direction (Fig. 4b). Similar behaviors have been reported in the noble gas bombardment of other covalently-bond structures [34,38,40]. Our kinetic Monte Carlo model is only able to capture the evolution of microscale surface features since any nanoscale mechanisms/features (from MD) are homogenized at the elemental level. Nevertheless, the microscale characteristic surface steps under an oblique ion incidence at steady state closely resemble the nanoscale terraced surfaces (each step spanning 10 to 100 nm) observed experimentally under relatively high angles of ion incidence and at high ion fluences [55,56]. This self-similarity suggests that similar mechanistic processes could govern the formation and evolution of these nanoscale features.

While the initial surface morphology does not control the steady-state sputtering yield, the transition time (fluence) to attain these steady-state structures is highly dependent on the initial surface roughness, as well as the ion incidence energy and angle. We show that

the fluence to attain steady-state sputtering yield under a normal ion incidence can be several-folds higher than under an oblique ion incidence, since any undulations have to be flattened completely under the former. Attaining steady-state sputtering yield under a normal ion fluence is therefore challenging, especially when the ion energies are low. While the exact xenon ion fluence used in obtaining the sputtering yield measurements in experiments is not widely reported, typical sputtering experiments are conducted over a period of 1 to 4 h, and in certain cases, over a maximum of 8 h [17]. This corresponds to an estimated fluence of $\sim 10^{18}$ to 10^{19} ions/cm^2 for a typical ion source, which is far short of the estimated $\sim 10^{19}$ to 10^{20} ions/cm^2 required to attain the characteristic steady-state structures in our simulations. Another source of uncertainty is the fluctuations in the steady-state sputtering yield under an oblique ion incidence, arising from the alternating decay of neighboring surface steps. The extent of such fluctuations depends on the density of these surface steps. Thus, the reported sputtering yield, even at steady-state, should be bounded by an uncertainty. The error bars in our Monte Carlo predictions, which account for the transient to steady-state variations in surface morphologies, are found to encompass a large portion of the experimental scatter across the range of ion energies and incidence angles.

Our simulations also show that the sputtering yield can be controlled to a certain extent by surface patterning. For example, periodic wall structures are found to reduce the sputtering yield under a normal ion flux by nearly two-fold, and the general morphology is maintained even under extended ion fluences. Under an oblique ion fluence, similar wall structures are found to lower the sputtering yield in the transient regime by several-folds. However, by acting as sacrificial elements, these wall structures eventually degrade to form surface steps, recovering back the steady-state sputtering yield. Such structural designs can enhance the sputter resistance capabilities of plasma facing materials, including the optics in ion thrusters, cathode and pole covers of Hall effect thrusters, as well as carbon wall panels of ground-based testing facilities for electric space propulsion [10,14–16]. Nevertheless, the nodes in our current one-dimensional Monte Carlo simulations only account for vertical changes in height and cannot model possible horizontal (sideway or out-of-plane) growth, which potentially could be important for accurately simulating the deposition of sputterants on tall vertical wall structures. Such two- or even three-dimensional (out-of-plane) Monte Carlo modeling is a subject of future work.

In summary, we have extended the length- and time-scales of MD simulations through a Monte Carlo model to elucidate the effects of the evolving surface morphology on the ion-surface sputtering mechanisms and resulting sputtering yield of carbon substrates. Regardless of the initial surface morphologies, our results show that the sputtered surfaces generally transition to a flat morphology under normal ion flux or form multiple surface steps under an oblique ion flux; the ensuing steady-state sputtering yield is insensitive to the initial surface morphology. However, initial surface structures can be engineered to reduce the sputtering yield under extended ion fluences in the transient regime, which have potential implications for lifetime extension of plasma facing components.

Declaration of Competing Interest

The authors declare that they have no known competing financial interests or personal relationships that could have appeared to influence the work reported in this paper.

Acknowledgement

This work is supported by NASA through the Joint Advanced Propulsion Institute, a NASA Space Technology Research Institute, under grant number 80NSSC21K1118. We acknowledge the use of computational resources under the Delta research computing project, which is supported by the National Science Foundation (award OCI 2005572), and the State of Illinois. Delta is a joint effort of the University of Illinois at Urbana-Champaign and its National Center for Supercomputing Applications. The use of the Advanced Cyberinfrastructure Coordination Ecosystem: Services & Support (ACCESS), through allocations MAT210031, MAT230055 and MSS22006, is also gratefully acknowledged.

Supplementary materials

Supplementary material associated with this article can be found, in the online version, at doi:10.1016/j.actamat.2023.119498.

Reference

[1] S.P. Kim, H.B. Chew, E. Chason, V.B. Shenoy, K.S. Kim, Nanoscale mechanisms of surface stress and morphology evolution in FCC metals under noble-gas ion bombardments, Proc. R. Soc. A. 468 (2012) 2550–2573, https://doi.org/10.1098/rspa.2012.0042.
[2] L. Xie, L. Jiao, H. Dai, Selective etching of graphene edges by hydrogen plasma, J. Am. Chem. Soc. 132 (2010) 14751–14753, https://doi.org/10.1021/ja107071g.
[3] M. Dvorak, W. Oswald, Z. Wu, Bandgap Opening by Patterning Graphene, Sci Rep 3 (2013) 2289, https://doi.org/10.1038/srep02289.
[4] A. Davydova, E. Despiau-Pujo, G. Cunge, D.B. Graves, Etching mechanisms of graphene nanoribbons in downstream H2 plasmas: insights from molecular dynamics simulations, J. Phys. D Appl. Phys. 48 (2015), 195202, https://doi.org/10.1088/0022-3727/48/19/195202.
[5] A. Harpale, H.B. Chew, Hydrogen-plasma patterning of multilayer graphene: mechanisms and modeling, Carbon N Y 117 (2017) 82–91, https://doi.org/10.1016/j.carbon.2017.02.062.
[6] A. Harpale, M. Panesi, H.B. Chew, Plasma-graphene interaction and its effects on nanoscale patterning, Phys. Rev. B. 93 (2016), 035416, https://doi.org/10.1103/PhysRevB.93.035416.
[7] E. Taglauer, Surface cleaning using sputtering, Appl. Phys. A. 51 (1990) 238–251, https://doi.org/10.1007/BF00324008.
[8] T. Šikola, L. Dittrichová, J. Spousta, J. Zlámal, J. Štefka, Cleaning of metal surfaces by a broad beam ion source, Nucl. Inst. Methods Phys. Res. Sect. B Beam Interact. Mater. Atoms 127–128 (1997) 865–868, https://doi.org/10.1016/S0168-583X(97)00022-0.
[9] J.N. Brooks, J.P. Allain, D.G. Whyte, R. Ochoukov, B. Lipschultz, Analysis of C-MOD molybdenum divertor erosion and code/data comparison, J. Nucl. Mater. 415 (2011) S112–S116, https://doi.org/10.1016/j.jnucmat.2010.08.061.
[10] D.M. Goebel, B. Jorns, R.R. Hofer, I.G. Mikellides, I. Katz, Pole-piece interactions with the plasma in a magnetically shielded hall thruster, in: Proceedings of the 10th AIAA/ASME/SAE/ASEE Joint Propulsion Conference, American Institute of Aeronautics and Astronautics, 2014, https://doi.org/10.2514/6.2014-3899.
[11] A. Hakola, J. Likonen, A. Lahtinen, T. Vuoriheimo, M. Groth, H. Kumpulainen, M. Balden, K. Krieger, M. Mayer, T. Schwarz-Selinger, S. Brezinsek, M. Kelemen, S. Markelj, M. Barac, S. Gouasmia, I.B. Radovic, A. Uccello, E. Vassallo, D. Dellasega, M. Passoni, M. Sala, E. Bernard, M. Diez, C. Guillemaut, E. Tsitrone, the A.U. Team, the Euro.M. Team, the Euro.W.P. Contributors, Gross and net erosion balance of plasma-facing materials in full-W tokamaks, Nucl. Fusion. 61 (2021), 116006, https://doi.org/10.1088/1741-4326/ac22d2.
[12] M. Patterson, M. Domonkos, J. Foster, T. Haag, L. Pinero, G. Soulas, Ion Propulsion Development Activities at the NASA Glenn Research Center, in: Proceedings of the 39th AIAA/ASME/SAE/ASEE Joint Propulsion Conference and Exhibit, American Institute of Aeronautics and Astronautics, 2003, https://doi.org/10.2514/6.2003-4709.
[13] R.B. Lobbia, J.E. Polk, R.R. Hofer, V.H. Chaplin, B. Jorns, Accelerating 23,000 h of ground test backsputtered carbon on a magnetically shielded hall thruster, in: Proceedings of the AIAA Propulsion and Energy 2019 Forum, American Institute of Aeronautics and Astronautics, 2019, https://doi.org/10.2514/6.2019-3898.
[14] P.M. Sforza, P.M. Sforza, Chapter 14 – space propulsion. Theory of Aerospace Propulsion, Butterworth-Heinemann, Boston, 2012, pp. 541–565, https://doi.org/10.1016/B978-1-85617-912-6.00014-1.
[15] G.C. Soulas, The impact of back-sputtered carbon on the accelerator grid wear rates of the NEXT and NSTAR Ion thrusters, in: Washington, D.C., 2013. https://ntrs.nasa.gov/citations/20150021367 (accessed October 31, 2022).
[16] G. Williams, T. Haag, J. Foster, J.V. Noord, S. Malone, T. Hickman, M. Patterson, Analysis of the pyrolytic graphite ion optics following the 2000-hour wear test of the HiPEP ion thruster, in: Proceedings of the 42nd AIAA/ASME/SAE/ASEE Joint Propulsion Conference & Exhibit, American Institute of Aeronautics and Astronautics, 2006, https://doi.org/10.2514/6.2006-5005.
[17] R. Deltschew, M. Tartz, V. Plicht, E. Hartmann, H. Neumann, Sputter characteristics of carbon-carbon compound material, in: Proceedings of the 27th International Electric Propulsion Conference, 2001.
[18] M. Tartz, Pyrolytic graphite and carbon-carbon sputter behaviour under xenon ion incidence, in: Proceedings of the 29th International Electric Propulsion Conference, 2005, p. 10.
[19] J.J. Blandino, D.G. Goodwin, C.E. Garner, Low energy sputter yields for diamond, carbon–carbon composite, and molybdenum subject to xenon ion bombardment,

Diam. Relat. Mater. 9 (2000) 1992–2001, https://doi.org/10.1016/S0925-9635(00)00350-2.
[20] R.P. Doerner, D.G. Whyte, D.M. Goebel, Sputtering yield measurements during low energy xenon plasma bombardment, J. Appl. Phys. 93 (2003) 5816–5823, https://doi.org/10.1063/1.1566474.
[21] J. Gruber, Low-energy sputter erosion of various materials in a T 5, in: Proceedings of the 27th International Electric Propulsion Conference, 2001.
[22] R. Kolasinski, J. Polk, D. Goebel, L. Johnson, Carbon sputtering yield measurements at grazing incidence, in: Proceedings of the 42nd AIAA/ASME/SAE/ASEE Joint Propulsion Conference & Exhibit, Sacramento, California, American Institute of Aeronautics and Astronautics, 2006, https://doi.org/10.2514/6.2006-4337.
[23] D. Rosenberg, G.K. Wehner, Sputtering Yields for Low Energy He^+-, Kr^+-, and Xe^+-Ion Bombardment, J Appl Phys 33 (1962) 1842–1845, https://doi.org/10.1063/1.1728843.
[24] J. Williams, M. Johnson, D. Williams, Differential sputtering behavior of pyrolytic graphite and carbon-carbon composite under xenon bombardment, in: Proceedings of the 40th AIAA/ASME/SAE/ASEE Joint Propulsion Conference and Exhibit, Fort Lauderdale, Florida, American Institute of Aeronautics and Astronautics, 2004, https://doi.org/10.2514/6.2004-3788.
[25] H. Tran, H.B. Chew, Surface morphology and carbon structure effects on sputtering: bridging scales between molecular dynamics simulations and experiments, Carbon N Y 205 (2023) 180–193, https://doi.org/10.1016/j.carbon.2023.01.015.
[26] R.D. Kolasinski, J.E. Polk, D. Goebel, L.K. Johnson, Sputtering yield measurements at glancing incidence using a quartz crystal microbalance, J. Vacuum Sci. Technol. A 25 (2007) 236–245, https://doi.org/10.1116/1.2435375.
[27] P. Sigmund, R. Behrisch, Sputtering by ion bombardment theoretical concepts. Sputtering By Particle Bombardment I, Springer Berlin Heidelberg, Berlin, Heidelberg, 1981, pp. 9–71, https://doi.org/10.1007/3540105212_7.
[28] R.M. Bradley, J.M.E. Harper, Theory of ripple topography induced by ion bombardment, J. Vacuum Sci. Technol. A 6 (1988) 2390–2395, https://doi.org/10.1116/1.575561.
[29] P.D. Shipman, R.M. Bradley, Theory of nanoscale pattern formation induced by normal-incidence ion bombardment of binary compounds, Phys. Rev. B. 84 (2011), 085420, https://doi.org/10.1103/PhysRevB.84.085420.
[30] O. Bobes, K. Zhang, H. Hofsäss, Ion beam induced surface patterns due to mass redistribution and curvature-dependent sputtering, Phys. Rev. B. 86 (2012), 235414, https://doi.org/10.1103/PhysRevB.86.235414.
[31] S. Habenicht, W. Bolse, K.P. Lieb, K. Reimann, U. Geyer, Nanometer ripple formation and self-affine roughening of ion-beam-eroded graphite surfaces, Phys. Rev. B. 60 (1999) R2200–R2203, https://doi.org/10.1103/PhysRevB.60.R2200.
[32] S. Habenicht, Morphology of graphite surfaces after ion-beam erosion, Phys. Rev. B. 63 (2001), 125419, https://doi.org/10.1103/PhysRevB.63.125419.
[33] S. Habenicht, K.P. Lieb, Diffusion and roughening during ion beam erosion of graphite surfaces, AIP Conf Proc 576 (2001) 951–954, https://doi.org/10.1063/1.1395461.
[34] I. Bizyukov, A. Mutzke, R. Schneider, A.M. Gigler, K. Krieger, Morphology and changes of elemental surface composition of tungsten bombarded with carbon ions, Nucl. Inst. Methods Phys. Res. Sec B Beam Interact. Mater. Atoms. 266 (2008) 1979–1986, https://doi.org/10.1016/j.nimb.2008.03.211.
[35] W. Boxleitner, G. Hobler, FIBSIM – dynamic Monte Carlo simulation of compositional and topography changes caused by focused ion beam milling, Nucl. Inst. Methods Phys. Res. Sec B Beam Interact. Mater. Atoms. 180 (2001) 125–129, https://doi.org/10.1016/S0168-583X(01)00406-2.
[36] G. Hobler, D. Kovač, Dynamic binary collision simulation of focused ion beam milling of deep trenches, Nucl. Inst. Methods Phys. Res. Sec B Beam Interact. Mater. Atoms. 269 (2011) 1609–1613, https://doi.org/10.1016/j.nimb.2010.12.076.
[37] D. Kunder, E. Baer, M. Sekowski, P. Pichler, M. Rommel, Simulation of focused ion beam etching by coupling a topography simulator and a Monte-Carlo sputtering yield simulator, Microelectron. Eng. 87 (2010) 1597–1599, https://doi.org/10.1016/j.mee.2009.11.007.
[38] A.S. Shumilov, I.I. Amirov, Profile Evolution of Silicon Nanostructures in Argon-Plasma Sputtering, J. Synch. Investig. 14 (2020) 935–943, https://doi.org/10.1134/S1027451020050195.
[39] M.V. Skachkov, Application of the Monte Carlo method for simulation of pattern formation by ion-beam sputtering of amorphous bodies, Math. Models Comput. Simul. 10 (2018) 551–563, https://doi.org/10.1134/S2070048218050113.
[40] A.S. Shumilov, I.I. Amirov, Morphology simulation of the surface subjected to low-energy ion sputtering, Tech. Phys. 60 (2015) 1056–1062, https://doi.org/10.1134/S1063784215070245.
[41] G.Z. Li, R.E. Wirz, Persistent Sputtering Yield Reduction in Plasma-Infused Foams, Phys. Rev. Lett. 126 (2021), 035001, https://doi.org/10.1103/PhysRevLett.126.035001.
[42] C.E. Huerta, T.S. Matlock, R.E. Wirz, Validation of a plasma-facing surface sputtering and deposition view factor model, in: Proceedings of the AIAA SPACE 2015 Conference and Exposition, Pasadena, California, American Institute of Aeronautics and Astronautics, 2015, https://doi.org/10.2514/6.2015-4503.
[43] C.E. Huerta, T.S. Matlock, R.E. Wirz, View factor modeling of sputter-deposition on micron-scale-architectured surfaces exposed to plasma, J Appl Phys 119 (2016), 113303, https://doi.org/10.1063/1.4944035.
[44] R.M. Bradley, G. Hobler, Sputter yields of surfaces with nanoscale textures: analytical results and Monte Carlo simulations, J Appl Phys 133 (2023), 065303, https://doi.org/10.1063/5.0137324.
[45] J.F. Ziegler, The stopping of energetic ions in solids, Nucl. Inst. Methods 168 (1980) 17–24, https://doi.org/10.1016/0029-554X(80)91225-2.
[46] W.D. Wilson, L.G. Haggmark, J.P. Biersack, Calculations of nuclear stopping, ranges, and straggling in the low-energy region, Phys. Rev. B. 15 (1977) 2458–2468, https://doi.org/10.1103/PhysRevB.15.2458.
[47] J.F. Ziegler, M.D. Ziegler, J.P. Biersack, SRIM – The stopping and range of ions in matter (2010), Nucl. Inst. Methods Phys. Res. Sec B Beam Interact. Mater. Atoms. 268 (2010) 1818–1823, https://doi.org/10.1016/j.nimb.2010.02.091.
[48] M. Titze, J.L. Pacheco, T. Byers, S.B. Van Deusen, D.L. Perry, D. Weathers, E. S. Bielejec, Evaluation of the accuracy of stopping and range of ions in matter simulations through secondary ion mass spectrometry and Rutherford backscattering spectrometry for low energy heavy ion implantation, J. Vacuum Sci. Technol. A 39 (2021), https://doi.org/10.1116/6.0001406.
[49] J.W. Wilson, F.A. Cucinotta, H. Tai, J.L. Shinn, S.Y. Chun, R.K. Tripathi, L. Sihver, Transport of light ions in matter, Adv. Space Res. 21 (1998) 1763–1771, https://doi.org/10.1016/S0273-1177(98)00063-5.
[50] H. Hofsäss, O. Bobes, Prediction of ion-induced nanopattern formation using Monte Carlo simulations and comparison to experiments, Appl. Phys. Rev. 6 (2019), 021307, https://doi.org/10.1063/1.5043188.
[51] C.C. Umbach, R.L. Headrick, K.C. Chang, Spontaneous nanoscale corrugation of ion-eroded SiO 2 : the role of ion-irradiation-enhanced viscous flow, Phys. Rev. Lett. 87 (2001), 246104, https://doi.org/10.1103/PhysRevLett.87.246104.
[52] M. Moseler, P. Gumbsch, C. Casiraghi, A.C. Ferrari, J. Robertson, The ultrasmoothness of diamond-like carbon surfaces, Science 309 (2005) 1545–1548, https://doi.org/10.1126/science.1114577.
[53] A.P. Yalin, J.D. Williams, V. Surla, K.A. Zoerb, Differential sputter yield profiles of molybdenum due to bombardment by low energy xenon ions at normal and oblique incidence, J. Phys. D Appl. Phys. 40 (2007) 3194, https://doi.org/10.1088/0022-3727/40/10/025.
[54] E. Oyarzabal, R.P. Doerner, M. Shimada, G.R. Tynan, Carbon atom and cluster sputtering under low-energy noble gas plasma bombardment, J. Appl. Phys. 104 (2008), 043305, https://doi.org/10.1063/1.2968549.
[55] M.P. Harrison, D.A. Pearson, R.M. Bradley, Emergence and detailed structure of terraced surfaces produced by oblique-incidence ion sputtering, Phys. Rev. E. 96 (2017), 032804, https://doi.org/10.1103/PhysRevE.96.032804.
[56] D.A. Pearson, R.M. Bradley, Theory of terraced topographies produced by oblique-incidence ion bombardment of solid surfaces, J. Phys. Condens. Matter. 27 (2014), 015010, https://doi.org/10.1088/0953-8984/27/1/015010.